Volume 13
Number 1
7 January 2025
Pages 1–812

Journal of Materials Chemistry A

Materials for energy and sustainability

rsc.li/materials-a

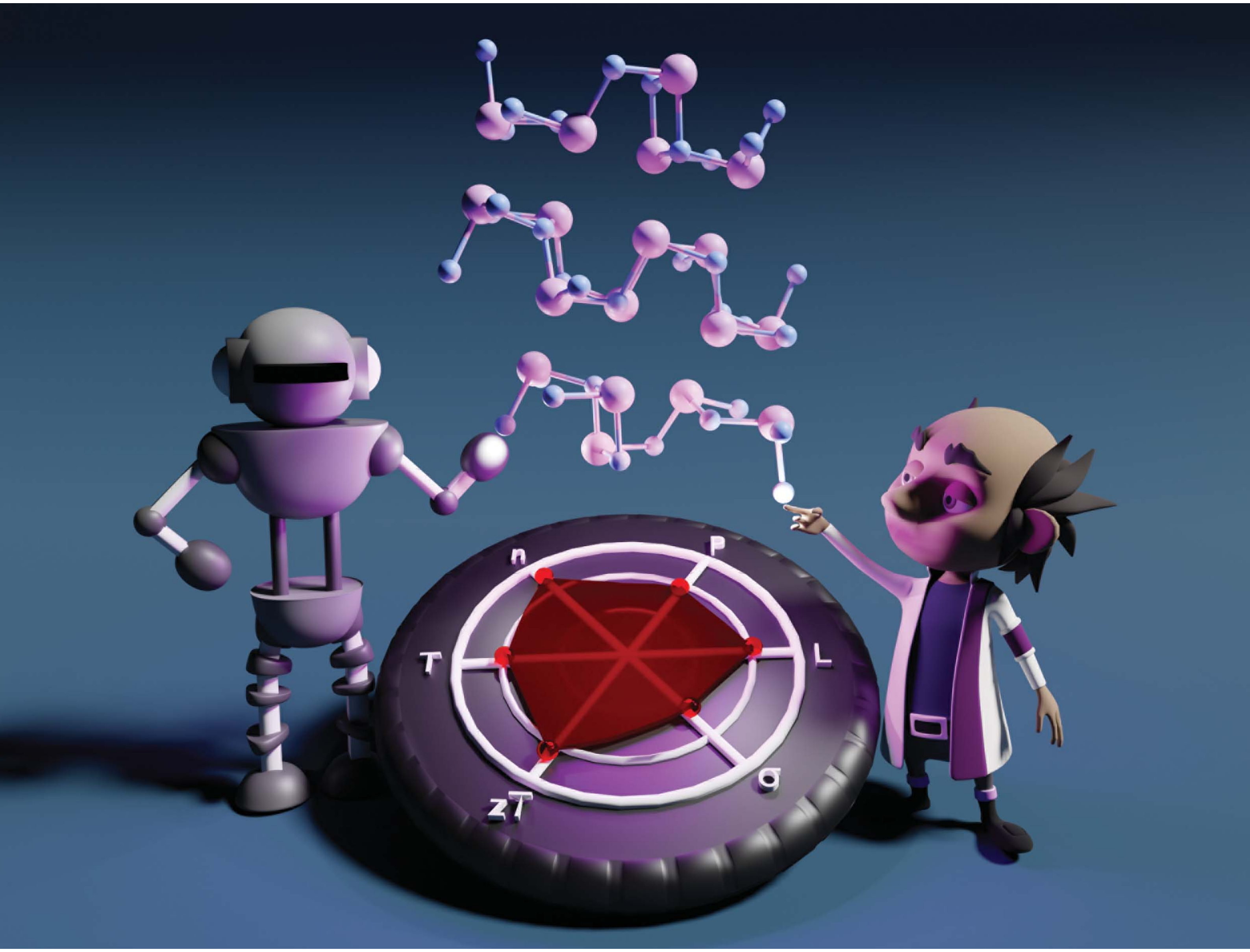

ISSN 2050-7488

ROYAL SOCIETY OF **CHEMISTRY**

PAPER
Jose J. Plata *et al.*
Enhancing the thermoelectric figure of merit of BiN *via* polymorphism, pressure, and nanostructuring

Journal of
Materials Chemistry A

PAPER

View Article Online
View Journal | View Issue

Check for updates

Cite this: J. Mater. Chem. A, 2025, 13, 220

Enhancing the thermoelectric figure of merit of BiN *via* polymorphism, pressure, and nanostructuring†

Elena R. Remesal, ‡[a] Victor Posligua, ‡[a] Miguel Mahillo-Paniagua,[b]
Konstantin Glazyrin, [c] Javier Fdez. Sanz, [a] Antonio M. Márquez [a]
and Jose J. Plata *[a]

Received 22nd August 2024
Accepted 5th November 2024

DOI: 10.1039/d4ta05891g

rsc.li/materials-a

Materials discovery extends beyond the synthesis of new compounds. Detailed characterization is essential to understand the potential applications of novel materials. However, experimental characterization can be challenging due to the vast chemical and physical spaces, as well as the specific conditions required for certain techniques. Computational high-throughput methods can overcome these challenges. In this work, the transport and thermoelectric properties of the recently synthesized bulk BiN are explored, including the effects of temperature, pressure, carrier concentration, polymorphism and polycrystalline grain size. We find that the band structure is strongly dependent on pressure and the polymorph studied. Both polymorphs exhibit low thermal conductivity at 0 GPa, which rapidly increases when pressure is applied. Electronic transport properties can be finely tuned based on the effects of pressure and polymorph type on the band gap, carrier mobilities, and presence of secondary pockets. The thermoelectric figure of merit can reach values around 0.85 for both p- and n-type BiN if the power factor and lattice thermal conductivity are optimized at 600 K, making this material competitive with other well-known thermoelectric families, such as Bi_2Te_3 or PbX, in the low-to-medium temperature range.

Introduction

A significant proportion of technological breakthroughs rely on the discovery of new materials. Historically, three primary approaches have been used to develop new materials.[1] Some compounds are accidentally discovered through serendipity while pursuing other objectives. Others are created using rational design principles based on previous successes, predicting desired properties using theoretical models and then synthesizing them in the laboratory. However, major advancements rarely occur this way. Incremental advances seldom lead to groundbreaking applications. Meanwhile, there are compounds that remained unused for many years until their functionality and commercial potential were eventually recognized. Polyacetylene, for example, was initially thought to be a useless black powder until its conductivity properties were discovered in the 1970s, leading to significant advancements in organic electronics.[2] GaN, another example, was first synthesized in 1928 but remained relatively unknown until the 1980s when its potential for electronic and optoelectronic applications was stablished.[3]

The emergence of high-throughput experimental methods combined with artificial intelligence has speed up the pace in which new compounds are discovered and synthesized.[4] Autonomous laboratories are potentially capable of targeting new materials, designing the optimal synthetic routes, and performing their synthesis.[5] However, these new methodologies have already faced significant challenges in the characterization process,[6] not to mention that many sophisticated approaches, including thin film sputtering, high-pressure synthesis are still beyond the current capabilities of autonomous labs. This scenario reaffirms the importance of developing systematic, accurate, and robust experimental measurements and theoretical predictions of materials properties, in which materials are not merely approached as single compounds but more as platforms for future wide-ranging applications. The use of graphene in different applications such as water filtration, sensors, and optoelectronics or $CoSb_3$ as thermoelectric material underscore the significance of comprehensive characterization and its crucial role optimizing emerging materials for diverse uses. This task is particularly critical in certain areas, such as thermoelectricity, where the transport properties that determine their thermoelectric performance are highly sensitive to synthetic, processing, and *operando* conditions. In addition to the challenge of covering a wide range of

---

[a] Departamento de Química Física, Facultad de Química, Universidad de Sevilla, Seville, E-41012, Spain. E-mail: jplata@us.es

[b] Research, Technological Innovation and Supercomputing Center of Extremadura (CenitS), Cáceres, Spain

[c] Photon Sciences, Deutsches Elektronen-Synchrotron, Notkestr. 85, 22607 Hamburg, Germany

† Electronic supplementary information (ESI) available. See DOI: https://doi.org/10.1039/d4ta05891g

‡ These authors contributed equally to this work.

parameters, experimental characterization techniques require specific conditions that may not be compatible with the stability conditions of the materials.

The bulk structure of BiN is a good example of how exploring novel materials potentially exhibiting a wide range of phenomena, *e.g.* thermoelectrics, piezo and/or pyro-electrics requires the use of theoretical modeling. Here and below we focus on BiN thermoelectric performance. While 2D BiN has been attracting attention for its potential use in transistor technology,[7] its bulk structure and properties have remained a mystery for a century after the first reported synthesis.[8] Glazyrin *et al.* recently synthesized and characterized two bulk BiN polymorphs at different pressures.[9] *Pbcn* BiN represents the stable polymorph at pressures higher than 12.5 GPa, whereas $Pca2_1$ is the prevailing phase under ambient conditions. The structural characterization of these compounds has revealed various features that make them candidates for thermoelectric materials. First, *Pbcn* BiN shares the same structural prototype as SnSe, which is one of the most efficient reported thermoelectric materials.[10] Bismuth is also a common element in thermoelectric materials due to its electron lone pair and the anharmonicity of its bonds with other elements.[11] Moreover, the difference in mass between Bi and N should increase the anharmonicity of the material and reduce its thermal conductivity. It is, however, difficult to experimentally characterize the thermoelectric properties of BiN due to its reactivity in the presence of O_2 or H_2O. In this work, DFT calculations are combined with Machine Learning to explore the transport properties of BiN bulk materials to determine its potential application as thermoelectric material, its deficiencies and venues for improvement.

Methodology

Thermal transport properties

Geometry optimization. DFT calculations were performed with VASP package,[12,13] using projector-augmented wave (PAW) potentials.[14] Energies were calculated with the exchange–correlation functional proposed by Perdew–Burke–Ernzerhof (PBE).[15] Core and valence electrons were selected following standards proposed by Calderon *et al.*[16] A dense *k*-point mesh of 2 × 4 × 2 *k*-points per reciprocal atom and a high-energy cutoff of 500 eV were used. Wavefunction was considered converged when the energy difference between two consecutive electronic steps was smaller than 10^{-9} eV. Geometry and lattice vectors were fully relaxed, using a 32 atoms conventional cell, until forces over all atoms were smaller than 10^{-7} eV Å^{-1}. An additional support grid for the evaluation of the augmentation charges was included to reduce the noise in the forces.

Supercell single-point calculations and force constants. Interatomic force constants, IFCs, were calculated using the hiPhive package, which combines the forces calculated for random atomic distortion in supercells with machine learning regression.[17] The forces were calculated in a 2 × 4 × 2 supercell (512 atoms) using the same setup as the one used for the geometry optimizations. The amplitude of the distortions applied to the atoms plays an important role in the calculation of the IFCs so a 2 steps approach was designed.[18] First, small random distortions were generated for all the atoms of three supercells and second and third-order IFCs were extracted using the hiPhive package. Then, 50 new distorted supercells were created superimposing normal modes with random phase factors and amplitudes corresponding to 300 K, using the second-order IFCs obtained in the previous step. The force constants were calculated from multi-linear regression to the DFT forces with the recursive feature elimination, RFE, algorithm. Although RFE is more expensive than using ordinary least-square regression, it has been proved that this algorithm requires a fewer number of structures to converge.[19] Additionally, reducing the number of parameters *via* RFE also simplifies the model, keeping only the most relevant interaction terms. To ensure compatibility at different pressures and polymorphs, cutoffs were determined based on coordination shells. The second-order terms include all interactions within the 2 × 4 × 2-supercell. The third and fourth-order force constant cutoffs vary slightly depending on the polymorph and pressure. For instance, the third and fourth-order force constants interatomic cutoffs are 5.3 and 3.2 Å, respectively, for the $Pca2_1$ polymorphs at 0 GPa.

Boltzmann transport equation, BTE, solver. ShengBTE code is used to calculate the lattice thermal conductivity, κ_l, through the iterative solution of the BTE, which produces better results than the relaxation time approximation.[20] Scattering times were computed including isotopic and three-phonon scattering. Memory demand and the convergence of κ_l with the number of *q*-points were balanced using a Gaussian smearing of 0.1 and a dense mesh of 12 × 12 × 12 *q*-points.

Electronic transport properties

Electrical conductivity, the Seebeck coefficient, and the electronic contribution to the thermal conductivity were calculated using the AMSET package.[21] This code solves the Boltzmann transport equation using the Onsager coefficients to predict electronic transport properties with the wavefunction from a DFT calculation as the main input. Scattering rates for each temperature, doping concentration, band, and *k*-point are calculated including scattering due to deformation potentials, polar optical phonons, and ionized impurities. Wavefunction coefficients were obtained using the HSE06 functional proposed by Heyd *et al.*,[22] using the primitive cell (32 atoms) and a dense mesh of 6 × 12 × 6 *k*-points. Elastic constants and deformation potential, required to compute the different scattering contributions were computed using the same setup used for the geometry optimization and force constants calculations. More details on how the thermal transport properties are incorporated into our high-throughput framework can be found in our previous studies.[23,24]

Results and discussion

Electronic band structure

We investigated the electronic band structure of both polymorphs, $Pca2_1$ and *Pbcn*, under varying pressure conditions. To ensure accuracy and consistency across our calculations, we employed a uniform dense *k*-point mesh, which was also utilized for the geometry optimization. We observed that the band gap value (E_g) decreases in both polymorphs by approximately 0.4 eV as pressure is increased from 0 to 12.5 GPa, in good agreement with Glazyrin *et al.*[9] Our electronic band structure provides additional details. At 0 GPa (Fig. 1a and c), both polymorphs exhibited flat valence bands (VBs), indicating low mobility and large effective masses (Table 1). However, when the pressure was increased to 12.5 GPa (Fig. 1b and d), a slight curvature in the VBs was detected, suggesting increased mobility in both $Pca2_1$ and *Pbcn* polymorphs. This effect is also observed in a reduction of the effective masses with increasing pressure.

The decrease in E_g values with increasing pressure in our study can be explained by the general reduction in interatomic distances within the materials.[25–27] This reduction typically leads to increased overlap between electronic orbitals, which in turn affects the energy levels of the VBs and conduction bands (CBs). As the atoms are pushed together, the energy separation between these bands decreases, resulting in a narrower band gap. This phenomenon is commonly observed in semiconductors and insulators under high-pressure conditions.[28–30] However, it is important to note that the behavior of E_g under pressure can vary depending on the specific material system. In some other systems, E_g can increase with pressure due to different electronic structure modifications.[31–33]

Furthermore, the curvature observed in the CBs is higher than that in the VBs. This increased curvature in the CBs suggests lower effective masses, which may influence the electron mobility (μ) in both polymorphs. Higher curvature typically indicates higher μ, as electrons can move more freely within the CB. Consequently, this effect would also impact the electrical conductivity (σ) of the material, as μ is directly related to σ. Therefore, the increased curvature of the CBs under pressure suggests that both μ and σ would be affected proportionally in both polymorphs. These implications for σ will be discussed in the following section, where we analyse the results obtained for the electronic transport properties of these systems.

Table 1 Effective masses of electrons, m_e, and holes, m_h, in units of the free electron mass for BiN polymorphs at different pressures

		m_h			m_e		
Pressure	SG	[100]	[010]	[001]	[100]	[001]	[001]
0 GPa	$Pca2_1$	−1.97	−1.03	−0.70	0.36	0.54	0.49
	Pbcn	−3.84	−1.45	−2.10	0.01	0.14	0.90
12.5 GPa	$Pca2_1$	−0.473	−0.453	−0.32	0.17	0.93	0.15
	Pbcn	−3.57	−1.64	−0.89	1.44	0.11	0.25

Thermal conductivity analysis

Thermal transport is explored on both polymorphs, calculating thermal conductivity (κ), a crucial property for understanding the efficiency of materials in thermoelectric applications, as it influences how well a material can conduct heat. Lattice thermal conductivity (κ_l) is described first because: (i) the moderate band gap of these materials makes phonon heat conduction the primary mechanism for heat transport at low and medium temperatures, and (ii) (κ_l) can be more easily tailored compared to the electronic contribution (κ_e), which is strongly coupled to electrical conductivity by the Wiedemann–Franz law.

For both $Pca2_1$ and *Pbcn* polymorphs, we observed that κ_l decreases with increasing temperature (Fig. 2). This behavior is

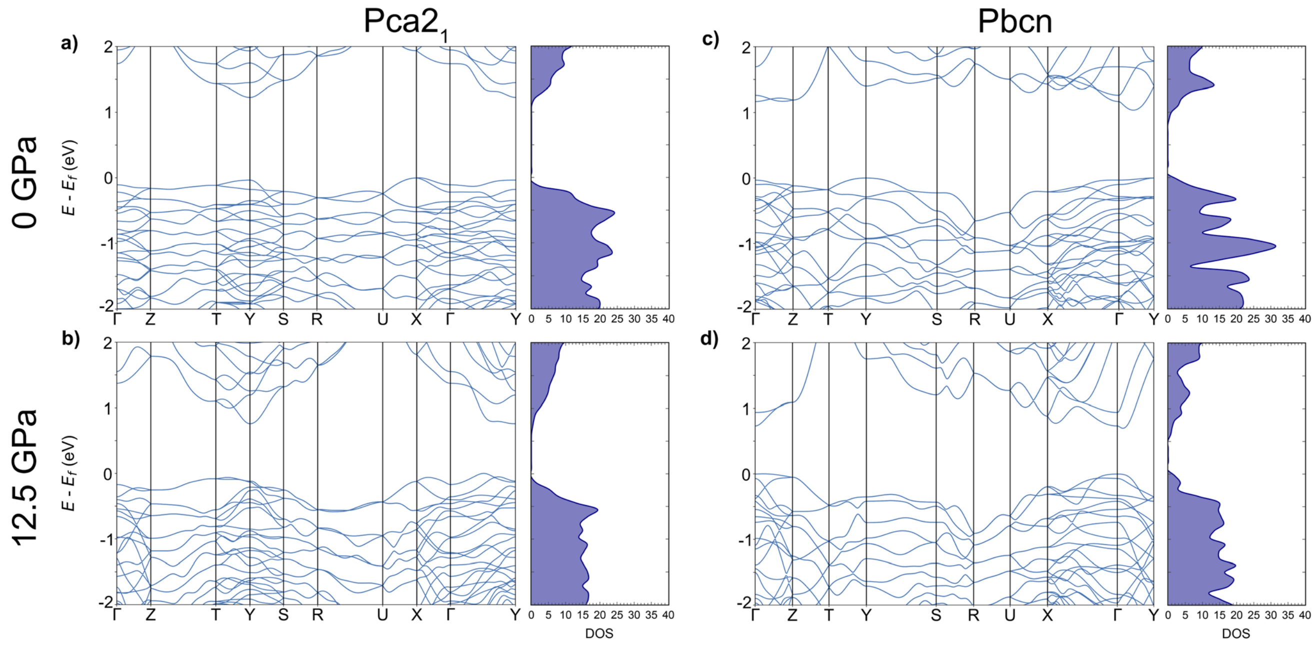

Fig. 1 Electronic band structures and density-of-states, DOS, for $Pca2_1$ (a and b) and *Pbcn* (c and d) polymorphs at 0 and 12.5 GPa.

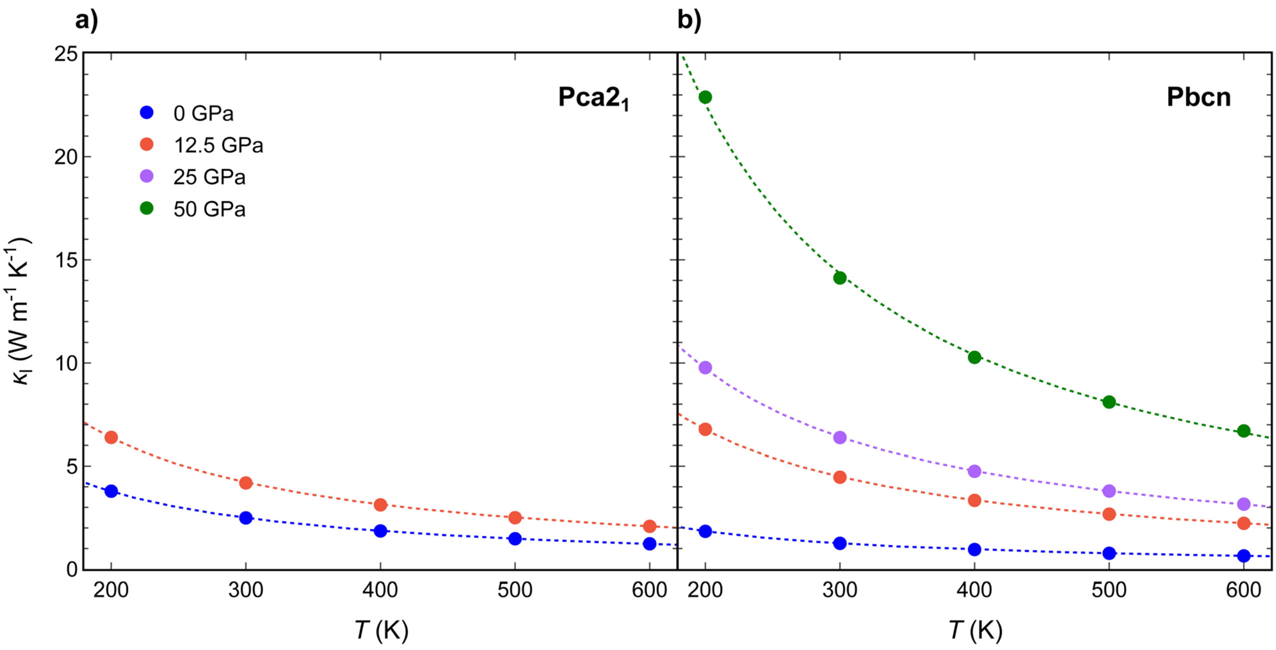

Fig. 2 Temperature variation of lattice thermal conductivity (κ_l) for (a) *Pca*2_1 and (b) *Pbcn* polymorphs at 0 (blue), 12.5 (orange), 25 (purple) and 50 (green) GPa.

typical in semiconductors due to increased phonon–phonon scattering rates at higher temperatures. This, in turn, reduces the mean free path of phonons, decreasing κ_l.[34–36] The lattice thermal conductivity is dominated by phonon–phonon Umklapp scattering, resulting in a T^{-1} dependence that reflects the increasing number of phonons available for scattering as the temperature rises.

Interestingly, at 0 GPa, *Pbcn* polymorph exhibits lower κ_l compared with *Pca*2_1, while at 12.5 GPa, κ_l values of *Pbcn* are higher than that of *Pca*2_1. This observation can be attributed to the differences in the group velocities between the two polymorphs (Fig. 3a and c). Our analysis revealed that the group velocities obtained for *Pbcn* polymorph are consistently higher than those of *Pca*2_1, with the values at 12.5 GPa being approximately three times higher at the 4–8 THz frequency range. This suggests that phonons in *Pbcn* polymorph exhibit faster propagation speeds, leading to enhanced thermal transport and higher κ_l compared to *Pca*2_1, particularly at higher pressures.

The scattering rates (W) are illustrated in Fig. 3b and d for *Pca*2_1 and *Pbcn* polymorphs, respectively. Both polymorphs display low scattering rates at low frequencies, where acoustic modes are predominant and serve as the primary contributors to the thermal conductivity of these materials. However, at 0 GPa, *Pbcn* polymorph presents higher values of W at these modes compared to the *Pca*2_1 polymorph. This explains the lower κ_l values for *Pbcn* polymorph at 0 GPa since higher scattering rates correspond to shorter phonon lifetimes and increased resistance to thermal transport. For *Pca*2_1 polymorph at 0 GPa, lower scattering rates allow for more efficient phonon transport, resulting in higher κ_l values compared to *Pbcn*. At 12.5 GPa, the situation is different: *Pca*2_1 polymorph exhibits similar values of W at low-frequency modes, however, κ_l is lower compared to *Pbcn*.

Further insight into the thermal conductivity behavior can be gained from examining the phonon dispersion curves for the *Pca*2_1 and *Pbcn* polymorphs at 0 and 12.5 GPa (Fig. 4). Additionally, the cumulative κ_l has been computed to understand the contribution of each vibrational mode to κ_l. The dispersion curves provide useful information to understand the group velocities and scattering rates discussed previously. At 0 GPa, both polymorphs present similar dispersion curves, with a first band containing acoustic and low-frequency optic modes in the 0–4.5 THz range, a second optical band around 6–9 THz, and a third optical band above 11 THz. Despite this similarity, their contribution to κ_l differs as can be deduced examining the cumulative contributions of each vibrational mode to κ_l. The main difference stems from the larger contribution of the first band to κ_l in the case of the *Pca*2_1 polymorph (around 1.83 W m^{-1} K^{-1}) compared to the *Pbcn* polymorph (0.81 W m^{-1} K^{-1}). As mentioned earlier, this difference is due to the *Pbcn* polymorph presenting higher values of W in this range of frequencies. The differences in κ_l between the two polymorphs are slightly diminished by the larger contribution to κ_l from the second optical band in the case of the *Pbcn* polymorph, primarily owing to its higher group velocities. This scenario completely changes at 12.5 GPa. Both polymorphs exhibit similar contributions to κ_l from the acoustic and low-frequency optical modes (3.53 W m^{-1} K^{-1} and 3.68 W m^{-1} K^{-1}). There is a significant shift of the second optical band in both polymorphs to higher frequencies, producing an overlap with the higher energy band. This shift is also connected to a strong increase in the group velocities, which significantly enhances their contribution to κ_l. For instance, for the *Pca*2_1 polymorph, the contribution of the

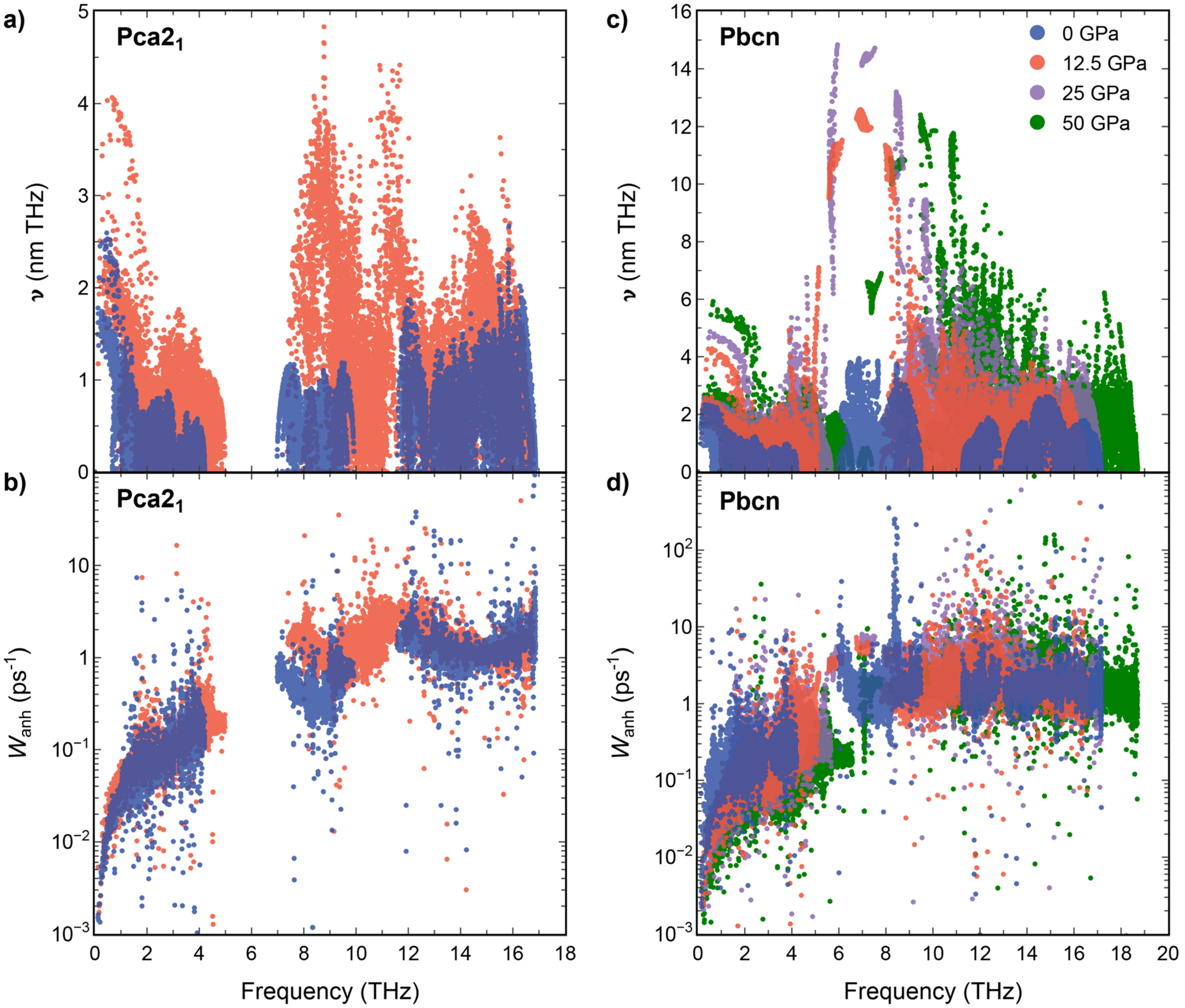

Fig. 3 Group velocities (a and c) and scattering rates (b and d) *vs.* frequency for *Pca*2$_1$ and *Pbcn* polymorphs at 0 (blue), 12.5 (orange), 25 (purple) and 50 (green) GPa.

second and third bands increases from 0.15 W m^{-1} K^{-1} to 0.65 W m^{-1} K^{-1} when pressure is changed from 0 GPa to 12.5 GPa. However, the main feature that changes the trend and makes the *Pbcn* polymorph present a higher κ_l than *Pca*2$_1$ at 12.5 GPa is the presence of two modes with exceptionally large group velocities in the region between 4.5–7.5 THz. Due to these large group velocities, these two modes contribute 0.73 W m^{-1} K^{-1} to κ_l, whereas this feature is not found in the *Pca*2$_1$ polymorph. The *Pbcn* polymorph also exhibits these high-velocity modes at higher pressures.

Electronic transport properties

To further elucidate the relationship between the structural, electronic, and transport properties of BiN, we investigated the electronic transport properties: power factor (PF), Seebeck coefficient (S) and electrical conductivity (σ) for both *Pca*2$_1$ and *Pbcn* polymorphs. Both p- and n-type BiN polymorphs have been explored in a large range of carrier concentrations (10^{17}–10^{20} cm^{-3}), at different temperatures (300–600 K) and pressures (0–12.5 GPa). This study did not investigate bipolar effects. To the best of our knowledge, AMSET is unable to simultaneously explore both electron and hole transport. However, bipolar effects are typically significant for materials with very narrow band gaps at high temperatures. In the present work, the lowest band gap obtained was around 0.4 eV, and the temperatures explored did not exceed 600 K, so bipolar effects are not expected to be dominant under the conditions investigated. As the thermoelectric figure of merit (zT) depends directly on the PF, first this magnitude will be explored then, its behavior will be analyzed as function of S and σ (Fig. 5).

Pressure appears to play a significant role in the transport properties of this material. The power factor is drastically increased when pressure is changed from 0 to 12.5 GPa, for both n-type and p-type as well as both polymorphs (Fig. 5a). This is

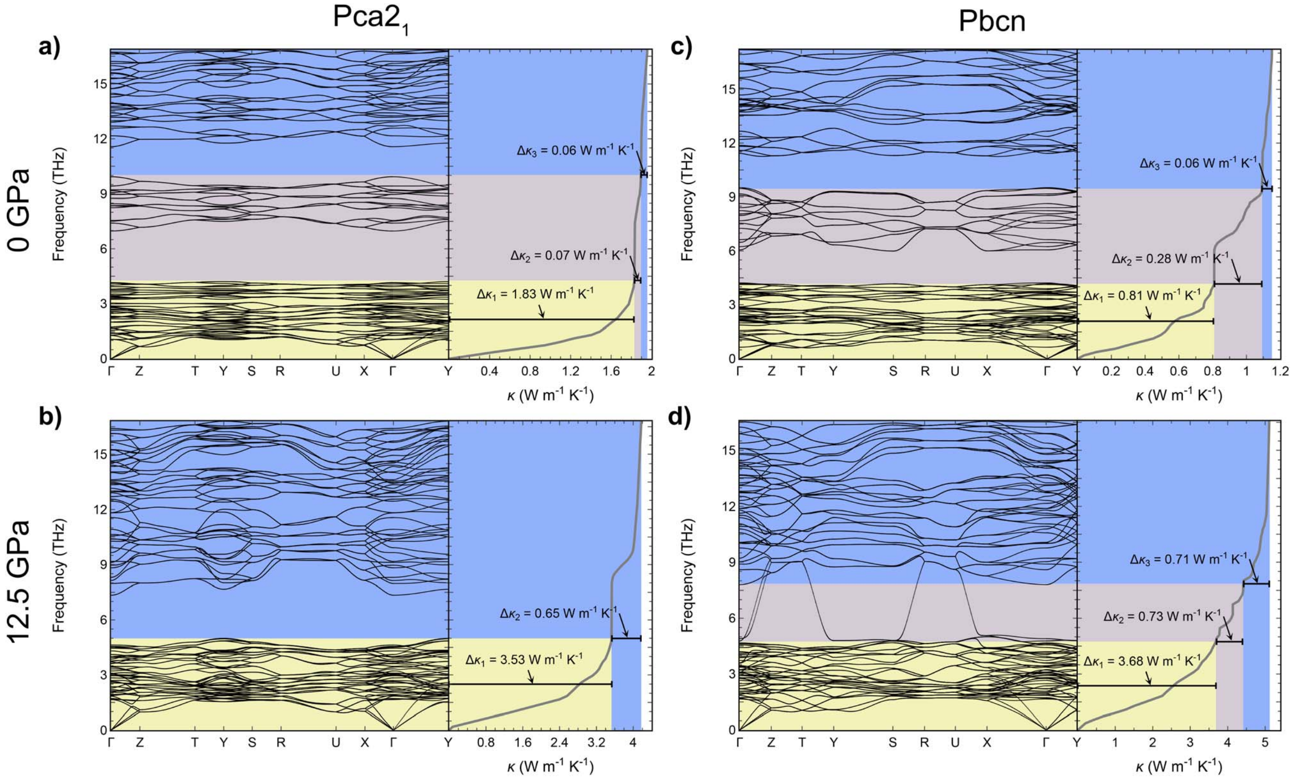

Fig. 4 Phonon dispersion curves and corresponding contributions to thermal conductivity (κ_l) for *Pca*2$_1$ (a and b) and *Pbcn* (c and d) polymorphs at 0 and 12.5 GPa. Right-side plots show the cumulative contributions to κ_l from different frequency ranges: $\Delta\kappa_1$, $\Delta\kappa_2$ and $\Delta\kappa_3$.

primarily due to a large increase in σ, in some cases around one order of magnitude, while the S is barely reduced (Fig. 5b). The large increase in σ can be analyzed based on the band structures discussed earlier. Pressure produces two main effects: it reduces the band gap of both polymorphs, and in some cases, it changes the curvature of the bands, thereby increasing the mobility of the charge carriers. Both of these phenomena contribute to the enhancement of σ.

Overall, n-type BiN exhibits a higher PF compared to its p-type counterpart. The larger electrical conductivity of n-type BiN, which is primarily responsible for its higher power factor compared to p-type, is strongly linked to its higher carrier mobility as indicated by the curvature of the conduction band edge. Furthermore, the enhancement of this trend with increased pressure can be attributed to not only the mobility increase, but also the creation of secondary carrier pockets with similar energy levels, particularly in the *Pbcn* polymorph. The presence of these secondary pockets is the reason why n-type BiN demonstrates exceptionally large PF values at higher temperatures (and specially at high carrier concentration).

The *Pca*2$_1$ polymorph exhibits slightly lower power factor values compared to the *Pbcn* polymorph for n-type behavior, but larger PF values for p-type behavior. Analyzing the band structure cannot explain this trend based solely on the band gap values. At 0 GPa, the *Pbcn* polymorph presents a lower band gap (1.03 eV) compared to *Pca*2$_1$ (1.22 eV). This trend is even more attenuated at 12.5 GPa, where the band gaps are reduced to 0.69 eV for *Pbcn* and 0.75 eV for *Pca*2$_1$. However, the presence of 2–3 different carrier pockets at the edge of the valence band of the *Pca*2$_1$ polymorph, which are very close in energy, explains the larger PF for the p-type *Pca*2$_1$ polymorph compared to *Pbcn*.

In summary, the electronic transport properties analysis reveals a complex behavior for BiN, which is influenced by temperature, carrier concentration, pressure, and polymorphism. There is a delicate balance between band gap, electron mobility, and secondary carrier pockets, and these factors can be tuned by the aforementioned variables to optimize the power factor of the material.

Figure of merit

Combining the analysis of thermal and electronic transport properties allows us to chart the thermoelectric figure of merit, zT, using variables such as temperature, pressure, carrier concentration, carrier type, and polymorph (Fig. 6 and 7). Due to the large band gap of this material, the electronic contribution to thermal conductivity, κ_e, is small enough at low and medium temperatures, so the lattice thermal conductivity κ_l is the main contributor to the total thermal conductivity κ. This is why some of the trends observed in the power factor PF analysis can be extrapolated to zT. For instance, n-type BiN exhibits higher zT than its p-type counterpart, and the *Pbcn* polymorph generally presents higher zT than the *Pca*2$_1$ polymorph. For single crystal BiN, n-type *Pbcn* shows a zT of approximately 0.8 at 600 K and a carrier concentration around 10^{20} cm^{-3}, while p-type *Pbcn* exhibits a zT of approximately 0.45 under the same

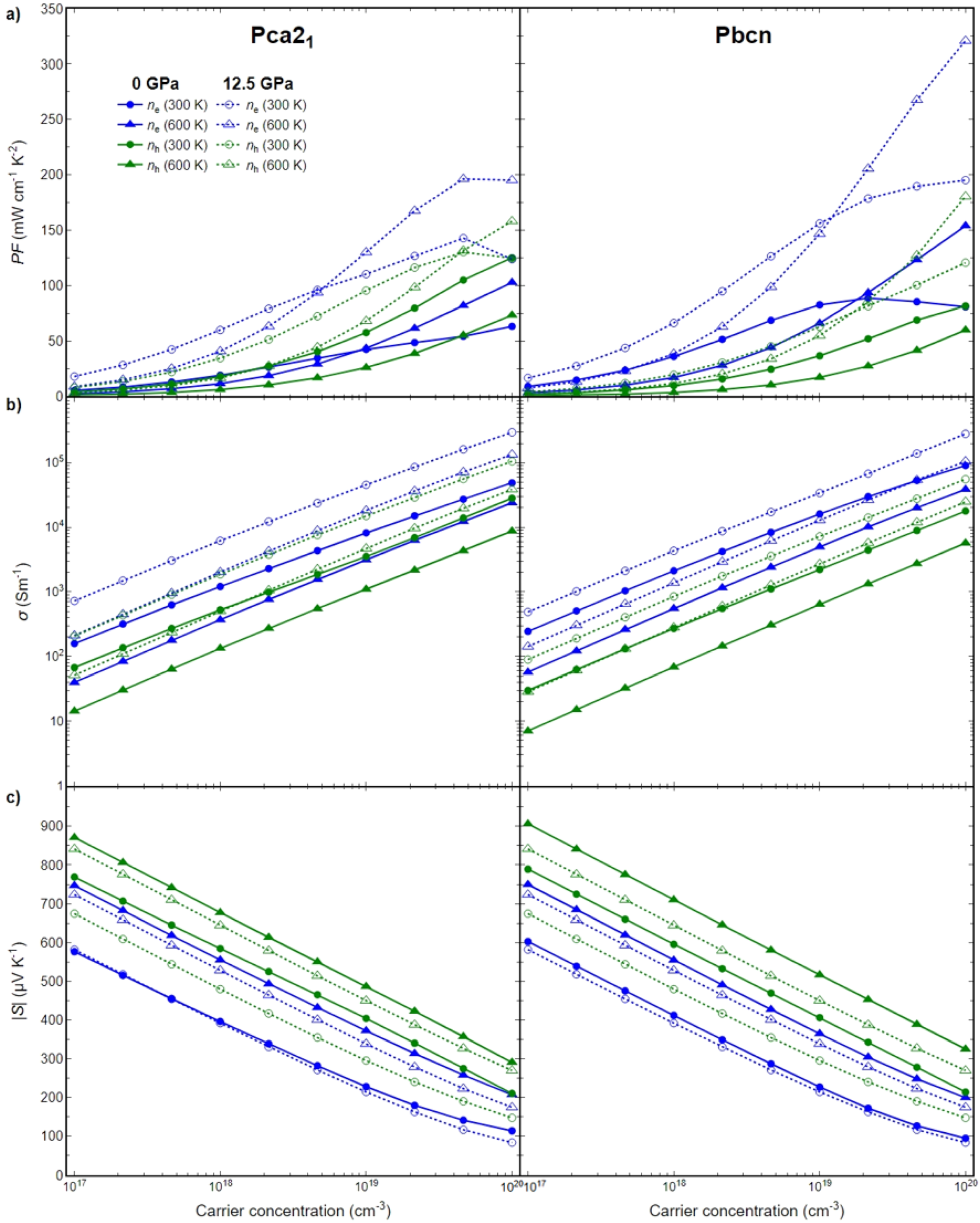

Fig. 5 (a) Power factor (PF), (b) electrical conductivity (σ), and (c) Seebeck coefficient (S) for *Pca*2_1 (left) and *Pbcn* BiN polymorph (right). Electronic transport properties are depicted in green and blue for p- and n-type, respectively. Circles and triangles are used for 300 K and 600 K. Properties at 0 GPa and 12.5 GPa are plotted in solid and dashed line, respectively.

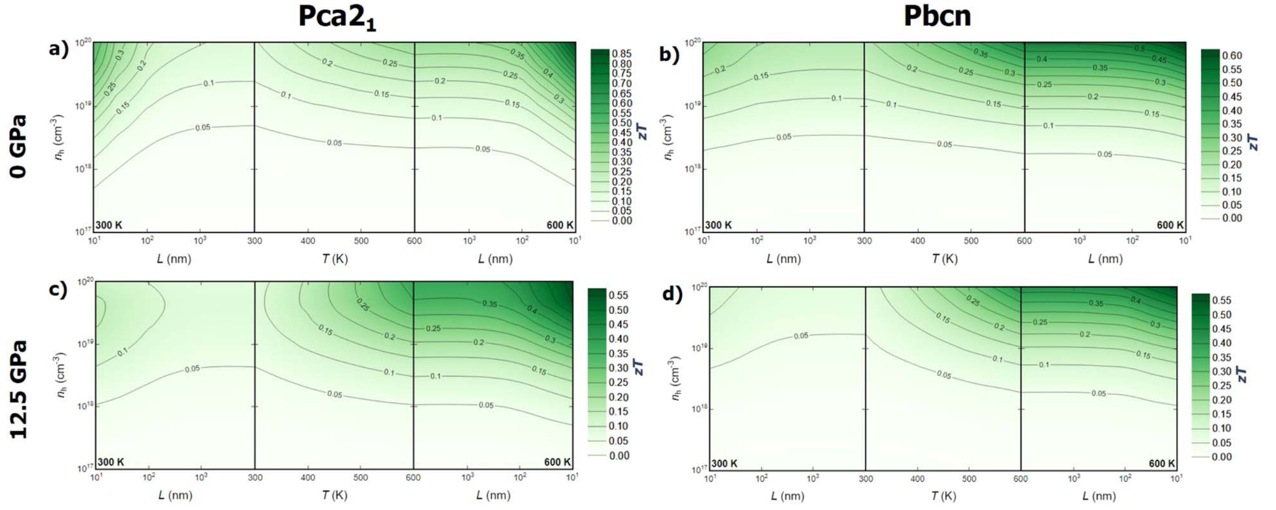

Fig. 6 Thermoelectric figure of merit (zT) for p-type BiN as function of temperature, carrier concentration and averaged grain size. (a and b) zT for $Pca2_1$ and $Pbcn$ polymorph at 0 GPa, respectively. (c and d) zT for $Pca2_1$ and $Pbcn$ polymorph at 12.5 GPa, respectively.

conditions. These values are slightly lower for the $Pca2_1$ polymorph, with values of 0.45 and 0.30 for n- and p-type, respectively, at 600 K.

Pressure is an interesting variable to consider. PF increases with pressure (Fig. 5a), but the lattice thermal conductivity κ_l also increases (Fig. 2). These trends balance each other, so zT values do not change drastically with increased pressure. Although the maximum zT values do not change significantly, there are important qualitative changes in the way zT is optimized. For single crystal p-type BiN at 0 GPa, the alignment of the contour lines parallel to the x-axis suggests that increasing the carrier concentration is the most effective route to enhance zT. At 0 GPa, both polymorphs exhibit low thermal conductivities, so the limiting factor is the carrier concentration in order to improve PF and, consequently, zT. When pressure is increased, κ_l increases substantially, so increasing the temperature to reduce this parameter also plays an important role. This fact drastically changes the shape of the contour lines and the approach to optimize zT. At high temperatures, maximizing zT requires not only increasing the carrier concentrations but also the temperature. A similar trend is observed for n-type BiN. As discussed earlier, n-type exhibits larger PF even at low carrier concentrations, which is why κ_l plays an important role at 0 GPa as well. When pressure is increased to 12.5 GPa, the main variable becomes temperature and $zT_{\max}$ can be obtained at moderate carrier concentration (5×10^{20} cm^{-3}) by increasing the temperature.

Optimizing the thermoelectric figure of merit, zT, of BiN requires considering additional variables beyond those discussed earlier. Until now, the predicted transport properties were considered for defect-free single crystals. However, most thermoelectric materials are synthesized and measured in

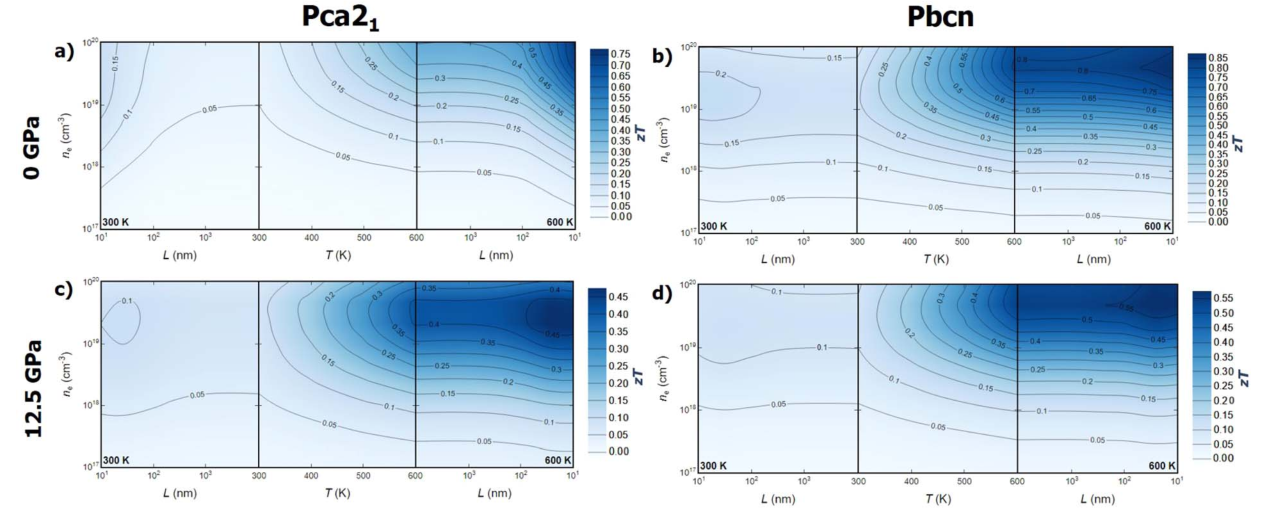

Fig. 7 Thermoelectric figure of merit (zT) for n-type BiN as function of temperature (T), carrier concentration (n) and averaged grain size (L). (a and b) zT for $Pca2_1$ and $Pbcn$ polymorph at 0 GPa, respectively. (c and d) zT for $Pca2_1$ and $Pbcn$ polymorph at 12.5 GPa, respectively.

polycrystalline form. Indeed, the microstructure plays a crucial role in determining the thermal and electronic transport properties of solids. Nanostructuring is a powerful strategy to optimize the thermoelectric efficiency of materials.[37] The ideal scenario is finding a size range where thermal conductivity is reduced while the power factor, PF, is maintained. The effect of grain size on thermal conductivity is discussed based on a decomposition of the contributions to κ_l by the phonon mean free path.[38] This approach has been widely used to theoretically investigate the nanostructuring effects on thermal transport in thermoelectric materials.[39–41] The value of κ_l for a particular particle size, L, is approximated as the cumulative contributions for all mean free paths up to L, effectively subtracting the contributions from mean free paths longer than the particle size. On the other hand, for the electronic transport properties, an extra term is included in the calculation of the electron/hole scattering rate, which is proportional to v/L, where v is the group velocity of the electron/hole. When average grain size is considered as a variable, a new trend emerges. While grain size does not appear to significantly affect the zT values for the *Pbcn* polymorph, zT is substantially increased for the *Pca*2$_1$ polymorph at grain sizes below 100 nm for both p- and n-type samples. For the p-type *Pca*2$_1$ polymorph of BiN, zT can more than double at 600 K when the grain size is around 50–60 nm. This suggests that the electron and phonon mean free paths are quite similar for the *Pbcn* polymorph, whereas the phonon mean free paths for the *Pca*2$_1$ polymorph are large enough to reduce the lattice thermal conductivity without significantly modifying the power factor, PF.

Conclusions

This work presents a comprehensive exploration of the thermoelectric properties of BiN. A high-throughput framework has been applied to efficiently explore the transport properties of BiN as a function of temperature, pressure, grain size, carrier concentration, type of conduction, and polymorph. The electronic transport properties of these systems are influenced by important changes in the band gap, electron/hole mobility, and presence of secondary carrier pockets. Overall, BiN exhibits higher power factor values for high-pressure and p-type samples. Additionally, the thermal transport properties appear to be very sensitive to the applied pressure. Lattice thermal conductivity increases with pressure but in different ways for both polymorphs. The presence of optical modes with large group velocities causes the *Pbcn* polymorph to increase its κ_l at a faster pace with pressure. When both electronic and thermal transport properties are combined, zT of this material can be explored. Different strategies to optimize zT can be extracted for the two polymorphs. zT values around 0.85 can be obtained for n-type *Pbcn* BiN at 600 K and 0 GPa, which suggests the need to find strategies to stabilize the high-pressure phase at 0 GPa/low pressures. On the other hand, both p- and n-type *Pca*2$_1$ polymorph can exhibit zT values around 0.6–0.7 for polycrystalline samples with an average grain size around 50–60 nm at 600 K and 0 GPa. These zT values are similar to those of other well-known thermoelectric families of materials in the low-to-medium temperature range, such as oxychalcogenides,[42] Bi_2Te_3,[43] or lead chalcogenides,[44] without toxic elements such Sb or Te, demonstrating the potential of undoped BiN for thermoelectric applications. Finally, but not the least, we note that chemical doping could further enhance thermoelectric performance, suggesting promising avenues for future research that will require a close collaboration between theory and experiment.

Data availability

Data sets are available at the ZENODO repository (**https://doi.org/10.5281/zenodo.14055923**).

Author contributions

J. J. P. and A. M. M. conceived and initiated the research project. E. R. R., M. M.-P. and V. P. performed all calculations. E. R. R., V. P. and J. J. P. performed all analysis presented in the main text, and wrote the first draft. K. G., A. M. M. and J. F. S. contributed to the data analysis and interpretation. A. M. M. and J. J. P. supervised the project. All authors discussed the results and contributed to the final paper.

Conflicts of interest

There are no conflicts to declare.

Acknowledgements

This work was funded by Spanish MICIN/AEI/10.13039/501100011033 and by European Union Next Generation EU/PRTR (grants TED2021-130874B-I00, PID2022-138063OB-I00). We thankfully acknowledge the computer resources at Lusitania and the technical support provided by Cénits-COMPUTAEX and Red Española de Supercomputación, RES (QHS-2023-1-0028).

Notes and references

1 A. K. Cheetham, R. Seshadri and F. Wudl, *Nature Synth.*, 2022, **1**, 514–520.
2 H. Shirakawa, E. J. Louis, A. G. MacDiarmid, C. K. Chiang and A. J. Heeger, *J. Chem. Soc. Chem. Commun.*, 1977, 578–580.
3 H. Amano, M. Kito, K. Hiramatsu and I. Akasaki, *Jpn. J. Appl. Phys.*, 1989, **28**, L2112.
4 D. P. Tabor, L. M. Roch, S. K. Saikin, C. Kreisbeck, D. Sheberla, J. H. Montoya, S. Dwaraknath, M. Aykol, C. Ortiz, H. Tribukait, C. Amador-Bedolla, C. J. Brabec, B. Maruyama, K. A. Persson and A. Aspuru-Guzik, *Nat. Rev. Mater.*, 2018, **3**, 5–20.
5 N. J. Szymanski, B. Rendy, Y. Fei, R. E. Kumar, T. He, D. Milsted, M. J. McDermott, M. Gallant, E. D. Cubuk, A. Merchant, et al., *Nature*, 2023, 1–6.
6 J. Leeman, Y. Liu, J. Stiles, S. Lee, P. Bhatt, L. Schoop and R. Palgrave, *ChemRxiv*, 2024, preprint, DOI: **10.26434/chemrxiv-2024-5p9j4**.

7 W. Zhou, S. Zhang, S. Guo, Y. Wang, J. Lu, X. Ming, Z. Li, H. Qu and H. Zeng, *Phys. Rev. Appl.*, 2020, **13**, 044066.

8 E. C. Franklin, *J. Am. Chem. Soc.*, 1905, **27**, 820–851.

9 K. Glazyrin, A. Aslandukov, A. Aslandukova, T. Fedotenko, S. Khandarkhaeva, D. Laniel, M. Bykov and L. Dubrovinsky, *Front. Chem.*, 2023, **11**, 1257942.

10 L.-D. Zhao, S.-H. Lo, Y. Zhang, H. Sun, G. Tan, C. Uher, C. Wolverton, V. P. Dravid and M. G. Kanatzidis, *Nature*, 2014, **508**, 373–377.

11 E. J. Blancas, J. J. Plata, J. Santana, F. Lemus-Prieto, A. M. Márquez and J. F. Sanz, *J. Mater. Chem. A*, 2022, **10**, 19941–19952.

12 G. Kresse and J. Hafner, *Phys. Rev. B: Condens. Matter Mater. Phys.*, 1993, **47**, 558–561.

13 G. Kresse and J. Furthmüller, *Phys. Rev. B: Condens. Matter Mater. Phys.*, 1996, **54**, 11169–11186.

14 P. E. Blöchl, *Phys. Rev. B: Condens. Matter Mater. Phys.*, 1994, **50**, 17953–17979.

15 J. P. Perdew, K. Burke and M. Ernzerhof, *Phys. Rev. Lett.*, 1996, **77**, 3865–3868.

16 C. E. Calderon, J. J. Plata, C. Toher, C. Oses, O. Levy, M. Fornari, A. Natan, M. J. Mehl, G. L. W. Hart, M. Buongiorno Nardelli and S. Curtarolo, *Comput. Mater. Sci.*, 2015, **108 Part A**, 233–238.

17 F. Eriksson, E. Fransson and P. Erhart, *Adv. Theory Simul.*, 2019, **2**, 1800184.

18 J. J. Plata, V. Posligua, A. M. Márquez, J. F. Sanz and R. Grau-Crespo, *Chem. Mater.*, 2022, **34**, 2833–2841.

19 E. Fransson, F. Eriksson and P. Erhart, *npj Comput. Mater.*, 2020, **6**, 135.

20 W. Li, J. Carrete, N. A. Katcho and N. Mingo, *Comput. Phys. Commun.*, 2014, **185**, 1747–1758.

21 A. Ganose, J. Park, A. Faghaninia, R. Woods-Robinson, K. Persson and A. Jain, *Nat. Commun.*, 2021, **12**, 2222.

22 J. Heyd, G. E. Scuseria and M. Ernzerhof, *J. Chem. Phys.*, 2006, **124**, 219906.

23 J. Santana-Andreo, A. M. Márquez, J. J. Plata, E. Blancas, J.-L. González-Sánchez, J. F. Sanz and N. Nath, *ACS Appl. Mater. Interfaces*, 2024, **16**, 4606–4617.

24 A. E. Rosado-Miranda, V. Posligua, J. F. Sanz, A. M. Márquez, P. Nath and J. J. Plata, *ACS Appl. Mater. Interfaces*, 2024, **16**, 28590–28598.

25 Y. Zhang, X. Jia, H. Sun, B. Sun, B. Liu, H. Lui, L. Kong and H. Ma, *J. Alloys Compd.*, 2016, **667**, 123–129.

26 N. V. Morozova, I. V. Korobeinikov and S. V. Ovsyannikov, *J. Appl. Phys.*, 2019, **125**, 220901.

27 Z. Jellil and H. Ez-Zahraouy, *Comput. Condens. Matter*, 2024, **38**, e00879.

28 K. Kaur and R. Kumar, *Chin. Phys. B*, 2016, **25**, 056401.

29 H. Aliabad and B. Yalcin, *J. Mater. Sci.*, 2017, **28**, 14954–14964.

30 H. Aliabad, S. Rabbanifar and M. Khalid, *Phys. B*, 2019, **570**, 100–109.

31 S. S. Essaoud, A. Bouhemadou, S. Maabed, S. Bin-Omran and R. Khenata, *Philos. Mag.*, 2022, **102**, 1522–1546.

32 D. Zou, Y. Liu, S. Xie, J. Lin, H. Zheng and J. Li, *RSC Adv.*, 2014, **4**, 54819.

33 J. Yue, S. Guo, J. Li, J. Zhao, C. Shen, H. Zhang, Y. Liu and T. Cui, *Mater. Today Phys.*, 2023, **39**, 101283.

34 M. G. Holland, *Phys. Rev.*, 1964, **134**, A471–A480.

35 T. Feng, L. Lindsay and X. Ruan, *Phys. Rev. B*, 2017, **96**, 161201.

36 J. Paterson, S. Mitra, Y. Liu, M. Boukhari, D. Singhal, D. Lacroix, E. Hadji, A. Barski, D. Tainoff and O. Bourgeois, *App. Phys. Lett.*, 2024, **124**, 181902.

37 M. G. Kanatzidis, *Chem. Mater.*, 2010, **22**, 648–659.

38 Z. Wang, J. E. Alaniz, W. Jang, J. E. Garay and C. Dames, *Nano Lett.*, 2011, **11**, 2206–2213.

39 A. Aziz, P. Mangelis, P. Vaqueiro, A. V. Powell and R. Grau-Crespo, *Phys. Rev. B*, 2016, **94**, 165131.

40 G. Romano, K. Esfarjani, D. A. Strubbe, D. Broido and A. M. Kolpak, *Phys. Rev. B*, 2016, **93**, 035408.

41 J. Plata, E. Blancas, A. Márquez, V. Posligua, J. Fdez Sanz and R. Grau-Crespo, *J. Mater. Chem. A*, 2023, **11**, 16734–16742.

42 S. D. Luu and P. Vaqueiro, *J. Materiomics*, 2016, **2**, 131–140.

43 I. T. Witting, T. C. Chasapis, F. Ricci, M. Peters, N. A. Heinz, G. Hautier and G. J. Snyder, *Adv. Electron. Mater.*, 2019, **5**, 1800904.

44 A. D. LaLonde, Y. Pei, H. Wang and G. J. Snyder, *Mater. Today*, 2011, **14**, 526–532.